

# Compound focusing mirror and X-ray waveguide optics for coherent imaging and nano-diffraction

Tim Salditt,<sup>a\*</sup> Markus Osterhoff,<sup>a</sup> Martin Krenkel,<sup>a</sup> Robin N. Wilke,<sup>a</sup>  
 Marius Priebe,<sup>a</sup> Matthias Bartels,<sup>a</sup> Sebastian Kalbfleisch<sup>a</sup> and Michael Sprung<sup>b</sup>

<sup>a</sup>Institut für Röntgenphysik, Universität Göttingen, 37077 Göttingen, Germany, and <sup>b</sup>DESY, Notkestrasse 85, 22607 Hamburg, Germany. \*Correspondence e-mail: tsaldit@gwdg.de

Received 27 February 2015

Accepted 20 April 2015

Edited by J. F. van der Veen

**Keywords:** coherent imaging; nano-diffraction; waveguides; holography.

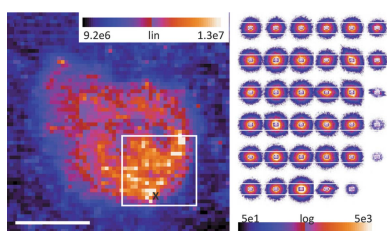
**Supporting information:** this article has supporting information at journals.iucr.org/s

A compound optical system for coherent focusing and imaging at the nanoscale is reported, realised by high-gain fixed-curvature elliptical mirrors in combination with X-ray waveguide optics or different cleaning apertures. The key optical concepts are illustrated, as implemented at the Göttingen Instrument for Nano-Imaging with X-rays (GINIX), installed at the P10 coherence beamline of the PETRA III storage ring at DESY, Hamburg, and examples for typical applications in biological imaging are given. Characteristic beam configurations with the recently achieved values are also described, meeting the different requirements of the applications, such as spot size, coherence or bandwidth. The emphasis of this work is on the different beam shaping, filtering and characterization methods.

## 1. Introduction

The advent of novel coherent X-ray imaging and microscopy techniques (Nugent, 2010; Quiney, 2010; Thibault & Elser, 2010) has created a need for optimized X-ray optical elements (Sakdinawat & Attwood, 2010; Schroer & Falkenberg, 2014) and systems delivering synchrotron radiation with desired coherence properties. For nanoscale resolution, the flux density has to be maximized by high-gain focusing, and at the same time the beam ('probe') has to be controlled in shape, wavefront, spectral content and coherence properties. Historically, nanoscale focusing of hard X-rays has been reached by very different and independent concepts, based on diffractive, refractive or reflective optics, as represented by the paradigmatic Fresnel zone plate, compound refractive lens or the elliptically curved Kirkpatrick–Baez (KB) focusing mirror. X-ray waveguides (WGs) have also created some early interest in view of nano-beam delivery (Feng *et al.*, 1993), and more recently in view of unique opportunities to control coherence, mode structure and wavefronts of guided waves (Zwanenburg *et al.*, 1999; Bergemann *et al.*, 2003; Bukreeva *et al.*, 2006; Osterhoff & Salditt, 2011). However, as isolated optical elements, the exit flux of two-dimensionally confining waveguide channels (Pfeiffer *et al.*, 2002) was found prohibitively low for imaging applications. More recently, combinations of different optical elements and compound optical systems have been used to optimize nanoscale focusing (Jarre *et al.*, 2005; Ruhlandt *et al.*, 2012; Döring *et al.*, 2013), which can include in particular a focusing and a filtering step (Jarre *et al.*, 2005; Giewekemeyer *et al.*, 2010; Krüger *et al.*, 2010).

In this work we describe a modular compound nano-focus optical system, composed of a high-gain fixed-curvature (KB) mirror and a probe filtering module, based on cleaning apertures and/or X-ray waveguides. Different advantages and



imaging modalities enabled by this optical system are demonstrated with representative applications. The optical approach has been implemented at the Göttingen Instrument for Nano-Imaging with X-rays (GINIX), installed at the P10 coherence beamline of the PETRA III storage ring at DESY in Hamburg, Germany. Instrumental settings and optical parameters of the endstation are detailed for matter of concreteness. We highlight three imaging modalities enhanced by the system: (i) near-field phase contrast imaging, also denoted as in-line holographic imaging, (ii) far-field coherent diffractive imaging (CDI) with ptychographic phase retrieval, and (iii) scanning nano-diffraction, in the small-angle or wide-angle regime (scanning SAXS/WAXS). The first two modalities [(i), (ii)] both yield the projected electron density of the object  $o(x, y)$ . However, the wavefield encoding  $o(x, y)$  is probed in very different diffraction regimes, far-field or near-field, depending on the object position, in the focal plane or at a defocus position, respectively. Both forms of coherent X-ray imaging overcome the requirement of model-based structure analysis by direct inversion of the diffraction data, but are governed by different properties of contrast transfer, phase retrieval, field of view and resolution. Near-field imaging (i) at high magnification and resolution relies on a nearly perfect quasi-spherical wavefront (probe), which imposes strong constraints on the probe preparation. One advantage of (i) over (ii) and also (iii) is that images can be recorded without scanning at variable field-of-view (FOV) and magnification. The last modality (iii) is closest to conventional diffraction studies, but with the added benefit of real-space resolution owing to the nanoscale beam size. The data are recorded in a tensor product space formed by two reciprocal dimensions and two real-space dimensions. The analysis is largely based on models and fitting of diffraction patterns in reciprocal space, as in conventional diffraction. In (iii) the real-space resolution is determined by the focal spot size, in contrast to (ii) CDI, where an oversampled far-field diffraction pattern is inverted by solving the phase problem. This was first achieved for the setting of a compact object with known support and coherent plane wave illumination (Miao *et al.*, 1999; Chapman *et al.*, 2006), and generalized later by ptychographic CDI (PCDI) to extended samples and non-idealized illumination (probe). Instead of a ‘compact object’, ptychography uses a compact probe and the partial overlap between illuminations of adjacent scan points to phase the diffraction pattern (Rodenburg *et al.*, 2007; Thibault *et al.*, 2008; Rodenburg, 2008). In its most advanced form, the constraint of separability allows for the reconstruction of both an unknown object  $o$  and unknown probe  $p$  (Thibault *et al.*, 2008).

The near-field or holographic imaging, denoted as modality (i) above, can be distinguished from the far-field case (ii) CDI, as usual in terms of the Fresnel number  $F = a^2/(\lambda z)$ , for given wavelength  $\lambda$  as a function of the propagation distance  $z$  to the detection plane. However,  $a$  may relate not only to a characteristic size of the object but equally to the probe (beam).

Hence it is often unclear how to use the Fresnel number in practice, and a better criterion to distinguish the regimes may be found by considering whether the detector receives signal

from the object’s scattered wave *and* the primary beam (i), or only the object’s scattered wave (ii). In the second case (ii) of far-field diffraction, the primary beam impinges only on the central detector pixels, which are excluded from analysis, *e.g.* when covered by a beamstop (BS) to protect the detector. Even if a semi-transparent central stop is used (Wilke *et al.*, 2013, 2014), the central pixels only ‘complement’ the ‘homodyne’ signal of the coherent diffraction pattern. This difference in how the signal is recorded entails a number of important consequences, concerning in particular the image and contrast formation, the scanning *versus* full-field character of the imaging mode, as well as the suitable phase retrieval/reconstruction algorithms. Most importantly, for the near-field or holographic approach (i), phase information of the scattered wave is directly encoded in the intensities by interference with the primary beam. By this holographic interference, a weak scattering amplitude can be amplified high above background signals of residual scatter, detector dark current or readout noise. In a hard X-ray nanofocus setup, the two modalities can both be accommodated by a simple change of sample location from a focus to a defocus position, as illustrated in Fig. 1. Along with this shift, an exchange of the detector is required, from a diffraction detector, *e.g.* single-photon-counting detector with large pixel size/large numerical aperture, to a high-resolution detector

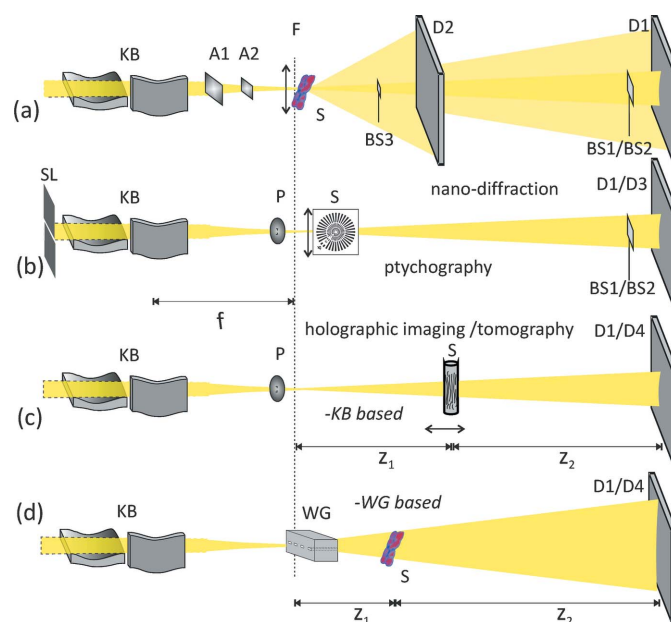


**Figure 1** Different imaging modalities supported by the compound optical system. (a) For scanning nanobeam diffraction, the partially coherent KB beam (open KB entrance slits) is cleaned by two successive soft-edge apertures (A1, A2) to cut the KB tails, and the diffraction is recorded by a SAXS (D1) and WAXS (D2) detector, each with respective beam stops (BS). (b) For ptychography, the KB beam is made fully coherent by closing the entrance slits, and the probe can be compactified by pinholes (P) if necessary for sampling. (c) For holographic imaging with the KB beam, the sample is moved to a defocus position, and, after alignment with the pixel detector (D1), a high-resolution detector (D4) is used to record the hologram. (d) For holographic imaging with highest resolution, an X-ray waveguide (WG) is used to filter the probe. Thereby, artifacts related to the typical wavefront distortions of a KB beam can be avoided.

with small pixel size, covering the radiation cone of the diverging primary beam.

The central optical element supporting all three imaging modalities described here as implemented at GINIX is the fixed-curvature KB mirror system. KB mirrors are well established as highly efficient focusing optics for hard X-rays (Hignette *et al.*, 2005; Matsuyama *et al.*, 2006; Mimura *et al.*, 2010). The high geometric acceptance and efficiency of KB mirrors enables unrivaled flux densities, while the relative large focal length, typically in the range  $f \simeq 0.1\text{--}0.4$  m, provides a working distance which is compatible with most sample environments. KB mirrors consist of two orthogonal elliptically figured reflecting surfaces, which focus the source (undulator exit or beamline secondary source) positioned in the first focal point to the nanofocus image in the second focal point. If the reflection is operated in total external reflection, the focusing scheme is essentially non-dispersive and allows for particularly high spectral bandwidth.

Record beam sizes below 50 nm in 2D (Matsuyama *et al.*, 2006) and 10 nm in 1D and 2D (Mimura *et al.*, 2010, 2011) have been reported, but most standard settings are designed to be in the range  $\Delta \simeq 100\text{--}500$  nm. Unless installed at very large distances behind the source (Takahashi *et al.*, 2010), most KB mirrors operate under conditions of partial coherence, since the geometric acceptance exceeds the spatial coherence length. However, at the expense of flux density, one can select the coherent fraction of the incoming beam with apertures

installed in front of the KB (Kewish *et al.*, 2010a; Giewekemeyer *et al.*, 2013). The resulting focal field is then fully coherent as required for coherent diffractive imaging (CDI) in the classical plane wave setting (sample smaller than  $\Delta$ ) or in the ptychographic setting (scanning diffractive imaging).

Two of the imaging modalities addressed here are also highlighted for their diagnostics purpose for the beam (probe). Firstly, for the fully coherent setting, we use ptychographic reconstruction of the focal or near-focal field distribution (Kewish *et al.*, 2010a,b; Schropp *et al.*, 2010; Guizar-Sicairo *et al.*, 2010, 2011; Mastropietro *et al.*, 2011; Hönig *et al.*, 2011; Giewekemeyer *et al.*, 2013, 2014; Wilke *et al.*, 2012, 2013, 2014). Secondly, for the partially coherent setting (fully opened KB entrance slits), waveguide optics are used to map out the intensity distribution in and around the focal plane.

## 2. Setup and waveguide optics

The GINIX endstation is installed in the second experimental hutch (EH2) of the PETRA III/P10 beamline. The beamline's optical path with components and distances from the 5 m undulator source are sketched in Fig. 2(a). The main components of the endstation, KB mirrors, cleaning and waveguide optics, sample stage, online optical microscopes for alignment and inspection, flight path and detector bench, are shown in Fig. 2(b), followed by schematics and micrographs describing the waveguide optics [Figs. 2(c)–2(g)]. The KB focusing system of GINIX provides an X-ray nano-focus for the photon energy range between 6 and 14 keV (Kalbfleisch *et al.*, 2011; Salditt *et al.*, 2011; Kalbfleisch, 2012; Bartels, 2013). Depending on orbit parameters, slit settings and alignment status, focal spot sizes down to about  $200\text{ nm} \times 200\text{ nm}$  (FWHM, as measured by waveguide scans) can be achieved with a flux larger than  $10^{11}$  photons  $\text{s}^{-1}$  (Salditt *et al.*, 2011). For reasons of space, the description of the optical parameters, instrumentation (optics, sample environment, detectors), coarse and fine alignment procedures for the KB and waveguide system, as well as experimental details such as energy stability of the focal spot, are deferred to the supporting information, and we only briefly comment on the waveguide optics uniquely available at the endstation.

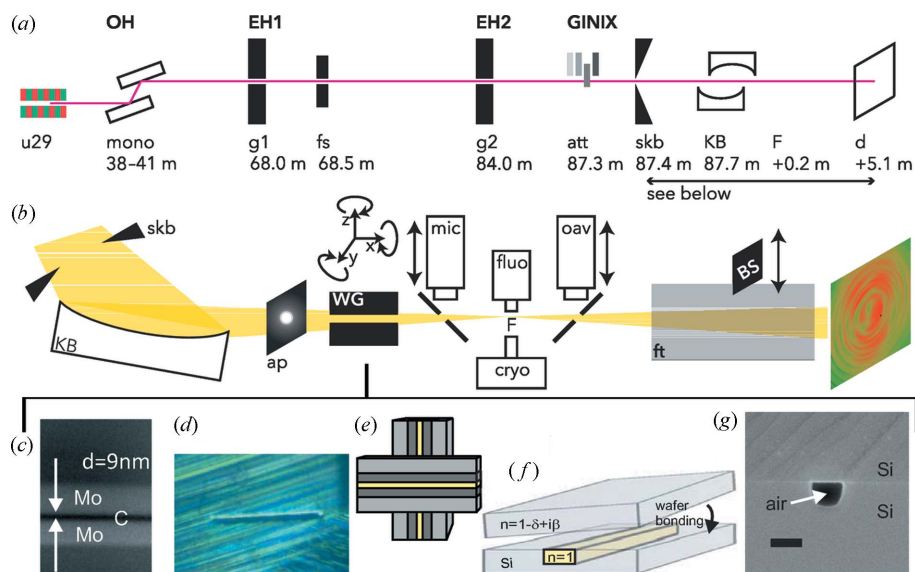


**Figure 2**

(a) Schematic of the P10 beamline and the GINIX endstation, with undulator (u29), double-crystal monochromator (mono), entrance slits (g1, g2) to the experimental hutches, fast shutter (fs), automated attenuators (att), KB clean-up slits (skb), the KB mirrors, the focal plane (F) and the detection plane (d), with the respective distances. (b) Close-up of the compound optical system with KB, beam selection aperture (ap), waveguide (WG), on-axis optical microscopes (mic, oav), an optional fluorescence detector (fluo), the cryojet sample environment (cryo), and the flight tube (ft) containing two beamstop holders (BS). (c) Electron micrograph of the sputtered thin-film sequence Ge/Mo/C/Mo/Ge used for the planar waveguide system (1DWG) (Krüger *et al.*, 2012). (d) The 1DWG as seen in the on-axis optical microscope with the relevant coupling region for the beam polished by a focused ion beam. (e) Schematic of a two-dimensional waveguide system (2DWG) realised by crossing two 1DWG slices. (f) Schematic of a lithographic waveguide channel (air) capped by wafer bonding (Neubauer *et al.*, 2014), with (g) a corresponding electron micrograph.

To insert the X-ray waveguides for holographic imaging or to scan through the KB focus for alignment and diagnostics, a custom-designed hexapod system (Smaract) is used. The centre of rotation can be conveniently shifted to the entrance of the waveguide, if needed selectively for each individual

channel of a waveguide chip. Two different waveguide systems are available. Firstly, a system of crossed sputtered coated planar thin-film waveguides with guiding layer made of C in the thickness range  $9 \text{ nm} \leq d \leq 80 \text{ nm}$ , and a two-component Ge/Mo cladding, optimized for high transmission in the spectral range  $11.1 \text{ keV} \leq E \leq 20 \text{ keV}$  (Salditt *et al.*, 2008; Krüger *et al.*, 2010, 2012). Secondly, 2D waveguide channels (air/vacuum) in silicon chips, fabricated by e-beam lithography, dry etching and wafer bonding (Giewekemeyer *et al.*, 2010; Neubauer *et al.*, 2014). Recent optimizations in design, fabrication and alignment resulted in a waveguide exit flux in the range  $I_{\text{WG}} \simeq O(10^8)\text{--}O(10^9) \text{ photons s}^{-1}$ , using the KB system of GINIX. The alignment of optical components (waveguides, clean-up pinholes) and of the samples is facilitated by two optical on-axis microscopes (Kalbfleisch, 2012; Bartels, 2013), which are directed parallel (pre-focus) and anti-parallel (post-focus) to the beam. Both microscopes are compatible with *in situ* X-ray recordings, but are also fully motorized ( $xyz$ ) to be moved out of the beam. As reflective optics, both KB and waveguides are essentially non-dispersive optical elements, and energy scans of the undulator and double-crystal monochromator can easily be performed with minimal realignment of the focusing system.

### 3. KB probe for ptychographic imaging

With a total coherent flux of up to  $I_0 \geq 10^{11}$  (Salditt *et al.*, 2011) and a spot size in the range 100–500 nm (depending on slit and alignment settings), a KB beam (probe) such as at the GINIX instrument offers a unique potential for ptychography in a high-flux/high-resolution setting. The probe can serve applications requiring a focused beam of high flux density in combination with a relatively large FOV, to be covered with a still moderate number of scan points, facilitating ptychographic tomography (Dierolf *et al.*, 2010; Wilke *et al.*, 2012). This setting entails a large super-resolution (*i.e.* ratio between resolution and spot size), and hence significant detector challenges. Here we discuss by which instrumentation this goal can be accomplished. Apart from imaging, we stress that ptychography is also an extremely powerful diagnostic tool at the beamline for studying the complex wavefield of the KB optics under varying illumination conditions (Giewekemeyer *et al.*, 2013). This is true at least for the parameter space which gives nearly full coherence (small slit settings and diffraction-limited probe), while the KB at full acceptance is only partially coherent and therefore requires other optical characterization techniques such as grating-based (Talbot) wavefront interferometry (Salditt *et al.*, 2011). It is commonly appreciated that ptychographic imaging offers a resolution better than the focal spot size, overcoming the lens-related limits of classical scanning transmission X-ray microscopy (Rodenburg *et al.*, 2007, 2008; Thibault *et al.*, 2008). Ptychography benefits from efficient focusing in view of increased flux density on the sample, pushing the cross-over from signal to noise towards high diffraction angles. The challenges, however, are mainly on the side of detectors. Sufficiently small pixel size, high count

rate and high dynamic range are indispensable to exploit this probe.

Concerning sufficient sampling of the diffraction pattern, a classical criterion for maximum allowable pixel size is given by the CDI oversampling criterion  $o = p\lambda/(zL) \geq 2$  (Miao *et al.*, 1999), which quantifies the sampling of the diffraction pattern for given wavelength  $\lambda$ , detector pixel size  $p$ , sample size  $L$  and distance  $z$  to the detector. The criterion warrants that each diffraction speckle is covered by at least two pixels in each direction, which limits the allowable sample size. Contrarily, ptychographic phase retrieval is compatible with unlimited sample size, but requires a compact probe, for which an equivalent sampling condition could be claimed, even if recent studies show that ptychography can tolerate under-sampling to some extent, so that this criterion may be overly restrictive [see for example Guizar-Sicairos *et al.* (2014) and references therein]. However, conservatively speaking, the beam size should be kept smaller than  $p\lambda/(2z)$ . It is important to note that ‘beam size’ in this context may not only designate the central width (FWHM) of the KB. In fact, a KB nano-focus is typically accompanied by pronounced tails which decay algebraically over distances exceeding the full width at half-maximum (FWHM) of the KB focal spot size  $\Delta_{x/y}$  by one to two orders of magnitude. These tails influence the speckles in the detection plane. In order to maintain sufficient sampling (with respect to the available  $p$ ), the KB beam can be ‘compactified’ by inserting pinholes fabricated by focused ion beam (FIB) milling (Giewekemeyer *et al.*, 2013). At GINIX, the tails of the focused beam were initially confined by either a large pinhole with 8  $\mu\text{m}$  diameter positioned at  $z_p \geq 4 \text{ mm}$  upstream from the focal plane, or a smaller pinhole of 1.4  $\mu\text{m}$ , positioned at  $z_p \simeq 0.5 \text{ mm}$ . Pinhole alignment was facilitated by the two on-axis visible-light microscopes upstream and downstream of the focal plane. After insertion of the pinholes, successful reconstructions became possible, but at the expense of restricted free range for the sample (for example, impeding cryogenic sample environments) and of reduced tolerance with respect to beam drifts.

More recently, the use of soft-edge apertures well in front of the focal plane has replaced the pinholes, and the beamline slit system g2 about 3 m in front of the KB is used to define the input pupil, while the slits directly in front of the KB housing serve for clean-up, yielding cleaner tails with minimized side lobes. With such optimized KB probe conditioning, the probe is now amenable to ptychographic reconstruction in the least invasive way without creating new ‘scatter’ due to apertures (Wilke *et al.*, 2015); see also Fig. 3 for a representative probe reconstruction at 13.8 keV under high-flux settings. An additional advantage is that the same soft-edge apertures can be used for ptychography and nano-diffraction, so that switching between the two configurations involves only slit and beam-stop settings.

Aside from sampling, the second technical challenge for ptychography with KB beams is related to the high flux and comparatively small cone beam angle, which delivers many photons into only a small number of detector pixels. This problem is much more severe for ptychography than for plane-

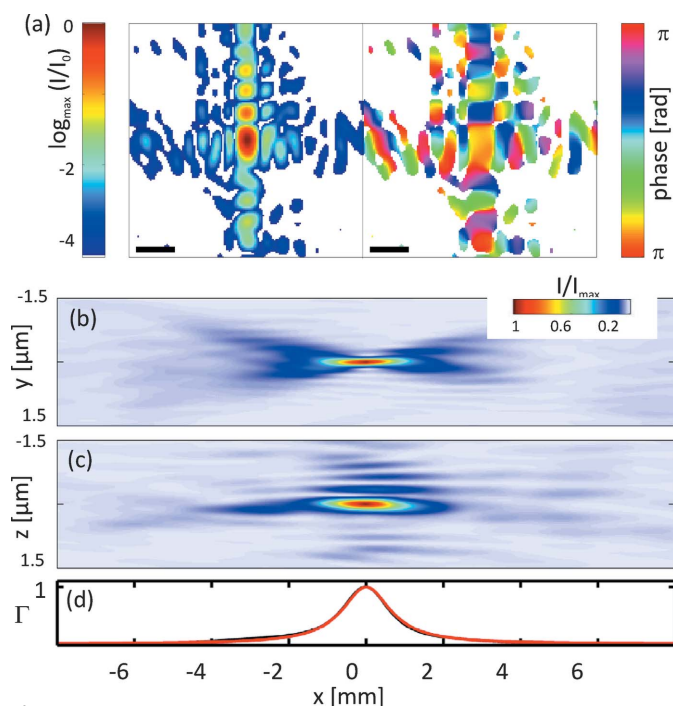


**Figure 3**

Ptychographic reconstruction of the KB probe at 13.8 keV with KB entrance slits  $100\ \mu\text{m} \times 100\ \mu\text{m}$ , reconstructed from data recorded by the Lambda detector and without pinhole [dataset 3 of Wilke *et al.*, 2015]. (a) Amplitude and phase are drawn according to the colourbar next to the image. Vertical and horizontal line-cuts through the intensity in the focal plane yield FWHM = 217 nm and FWHM = 136 nm, respectively. (b, c) Intensity distribution as calculated from numerical propagation of the reconstructed field, in the (b)  $yx$  and (c)  $zx$  planes. (d) Normalized sharpness as obtained from an area integral of the squared intensity, along with a Lorentzian fit, yielding a depth of focus of 1.53 mm (FWHM). Scale bar in (a): 500 nm.

wave CDI, since intensity values need to be recorded also in the centre of the diffraction pattern, and cannot be simply blocked by a ‘beamstop’. A seemingly simple and obvious solution to the problem of limited dynamic range is therefore the use of a semi-transparent central stop (STCS), covering just those pixels in the centre which are too ‘hot’. This solution has been recently implemented by specially designed single-crystal STCSs, with all calibration and rescaling issues properly addressed (Wilke *et al.*, 2013). For ptychography, the choice of detector is instrumental. The key property of modern pixel detectors, such as the commercially available Pilatus (Dectris) (Kraft *et al.*, 2009) with  $p = 172\ \mu\text{m}$  and Maxipix (ESRF) (Llopart *et al.*, 2002) with  $p = 55\ \mu\text{m}$ , is the capability of single photon counting with an effectively zero readout noise in combination with maximum count rates in the range  $10^5$ – $10^7$  photons  $\text{pixel}^{-1}\ \text{s}^{-1}$  (depending on the pixel size) (Trueb *et al.*, 2012). A more recent pixel detector development reaching kHz frame rates is the ‘Eiger’ (Johnson *et al.*, 2012) with  $p = 75\ \mu\text{m}$ , well suited for high-throughput ptychography (Guizar-Sicairos *et al.*, 2014). Further, the Large Area Medipix-Based Detector Array (Lambda) based on the Medipix3 chip offers  $p = 55\ \mu\text{m}$  and a frame rate up to 2000 frames  $\text{s}^{-1}$  based on two counters for dead-time-free readout (Pennicard *et al.*, 2012). For detection of still higher

flux density, hybrid detectors combine features of single-photon-counting (at low signal) and integrating counters (for high signal), such as the MM-PAD detector (Tate *et al.*, 2013), which was successfully tested for ptychography at count rates of  $10^8$  photons  $\text{pixel}^{-1}\ \text{s}^{-1}$  (8 keV) (Giewekemeyer *et al.*, 2014). Geared towards fast readout and smaller pixel size of  $55\ \mu\text{m}$ , the new Lambda detector was also used for ptychography applications at GINIX (Wilke *et al.*, 2015). In combination with optimized semi-transparent central stops, the high count rate of the detector has enabled reconstructions at an unprecedented flux density of  $10^5$  photons  $\text{nm}^{-2}\ \text{s}^{-1}$ . A further advantage of the Lambda detector is given by the partially sensitive pixels in the inter-module gaps, avoiding the missing data common for other pixel detectors. The small pixel size made it possible to achieve sufficient sampling also for higher photon energies than around 8 keV, notably for 13.8 keV, to dispense of the pinholes, and to open the slits used for KB illumination to  $100\ \mu\text{m}$ . The probe reconstruction resulting from this setting is shown in Fig. 3. For the scan, a Ta test sample (ATN/XRESO-50HC, NTT-AT, Japan) was scanned with 200 nm step size and 21 scan positions, with dwell time 50 ms (data not shown) (Wilke *et al.*, 2015).

#### 4. KB probe of scanning nanobeam-diffraction

Complementing optical fluorescence and electron microscopy, the emerging X-ray nano-diffraction and coherent imaging methods can help to shed light on unlabelled cellular structures in cells such as protein, fixed without slicing and staining, and even in live cells (Weinhausen *et al.*, 2012, 2014; Priebe *et al.*, 2014). Cellular biopolymer networks with associated motor proteins determine shapes, movements, elasticity and forces in cells and are also fascinating active soft matter systems. For a quantitative understanding and modelling, it is important to unravel the local structure of the biomolecular assemblies and networks. For example, the cytoskeletal actin network plays an essential role for directed cellular motion *via* actin polymerization/depolarization and bundling of filaments in the cortex. Scanning nano-beam diffraction combines high resolution in reciprocal space (by analysis of the diffraction patterns) with resolution in real space on the order of the beam size, *i.e.* for the present example in the range 200–400 nm, as defined by the KB focus, extending previous scanning SAXS experiments (Bunk *et al.*, 2009) to nanoscale resolution in real space. The method can hence probe local structures (in reciprocal space) in the range smaller than the beam size down to the length scale given by a signal-to-noise cut-off. This cut-off depends on the order in the sample and is typically intermediate between length scales of the organelle and the molecular constituents. Using the optical scheme of KB focusing and cleaning presented here, scanning X-ray diffraction microscopy of different cell lines was successfully implemented for different states and environments, from freeze-dried states to biologically more relevant states such as cryogenically fixed (Priebe *et al.*, 2014) as well as living hydrated cells (Weinhausen *et al.*, 2014; Priebe *et al.*, 2014). Notably, we have recently observed pronounced anisotropic

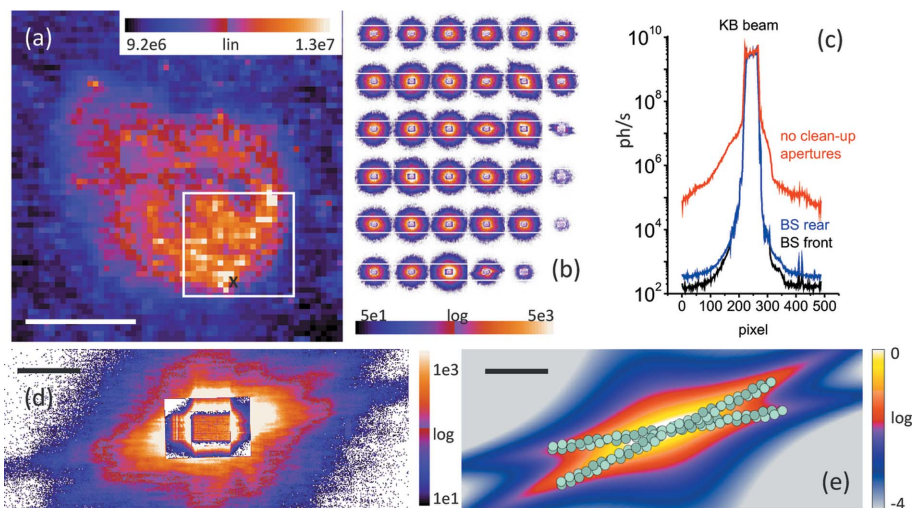
diffraction patterns in the cortex of migrating cells, which can be attributed to actin fibre bundles. In some cases, the local diffraction patterns consist of characteristic diffraction streaks very similar to what is observable for *in vitro* suspensions of actin and  $\alpha$ -actinin (Töpperwien, Priebe, Salditt *et al.*, unpublished). Such a signal could be explained by actomyosin fibre bundles oriented parallel to the cell-cortex. From automated analysis of the scanning diffraction data, the local anisotropy of the diffraction pattern can be determined, based on Fourier methods (Priebe *et al.*, 2014) or principle component analysis of the covariance computed for the 2D diffraction pattern.

Fig. 4 shows results obtained for a *Dictyostelium discoideum* cell, a well known social amoeba and genetically controlled model organism for eukaryotic cellular migration. The cells have been cryogenically fixated by rapid plunging of cells in ultra-cold ethane using a grid plunger (GP1, Leica) followed by sample transfer into the cryogenic jet at GINIX. In other similar measurements, chemical fixation and even live cell imaging in microfluidic chambers (ibidi, Munich) has also been used. Cells are then selected by the optical on-axis microscope. We found that the jet system, which is significantly simpler than cryogenic sample environments in vacuum, is fully compatible with scanning transmission X-ray microscopy and even with ptychographic coherent diffractive imaging. For the dark-field overview scan shown in Fig. 4(a), the sample is aligned and scanned in the  $E_\lambda = 7.9\text{keV}$  beam using a fast piezo stage. A full (small-angle) diffraction pattern is recorded at each pixel, and a darkfield map is generated by adding up

the entire scattering around a mask (central stop, residual KB streaks). The beam was focused to  $326\text{ nm (H)} \times 392\text{ nm (V)}$  (FWHM), with a total photon flux of  $I_0 = 1.1 \times 10^{11}$  photons  $\text{s}^{-1}$ , as measured with the Pilatus 300K, positioned 5.29 m behind the sample, which is placed in the focal plane of the KB. The local diffraction patterns exhibit a significant diversity which can be quantified in terms of anisotropy parameters and angularly averaged structure factors. The typical contrast modes extracted from the diffraction data by automated scripts created in this project are: dark-field, differential phase contrast and an anisotropy parameter (Priebe *et al.*, 2014). The anisotropy reflects the local orientation of actin bundles and was found to be consistent with the ring-like or arc-like regions of enhanced myosin-II/actin concentration (contractile ring) observed with fluorescence microscopy. Beyond the orientation and the scattering intensity, many structural parameters can be deduced from the data, further efforts in modelling provided. Future work has to be directed towards quantitative modelling of the diffraction signal in terms of fibre bundle parameters (geometry, spacing, number of filaments). As a first step, a model based on a bundle of cylindrical Gaussian ‘cigars’ has been used to simulate the decay of scattering intensity along the streak as a function of momentum transfer  $q_\perp$  (Priebe *et al.*, 2014). Some streaks exhibit pronounced modulations (depending on the position in the cell), indicative of positional correlations between parallel filaments in a bundle.

First experiments on living cells have demonstrated that it should be possible to capture live structure in isolated diffraction shots during cellular locomotion. Suitable microfluidic sample chambers for *in situ* nano-beam X-ray diffraction have been developed based on home-built microfluidic chips (Weinhausen & Köster, 2013) or based on adaptations of commercial cell culture slides (ibidi) (Bernhardt *et al.*, unpublished).

As a further example of nanobeam-diffraction, we present test measurements performed at GINIX on the myelin structure of sciatic neurons, isolated from wild-type mouse by a teased fibre preparation, to show the quality increase in the signal of the local diffraction patterns with respect to our earlier multimodal X-ray microscopy study (Ducic *et al.*, 2011). The myelin sheath is well known as the multi-lamellar membrane structure formed by glia cells and wrapping around the neural axons in particular of the peripheral nervous system (PNS). It ensures electrical insulation of axons and fast saltatory nerve conduction based on its segmental structure along the axon, segmented by the nodes of



**Figure 4**  
 (a) Dark-field overview scan of a frozen hydrated *Dictyostelium discoideum* cell with  $1\ \mu\text{m}$  step size and  $0.5\ \text{s}$  dwell time (continuous scan). Scale bar:  $10\ \mu\text{m}$ . (b) Exemplary far-field patterns recorded with  $10\ \text{s}$  accumulation time in an array of  $6 \times 6$  points in the region indicated by the white square in (a). While the diffraction patterns are radially symmetric in the centre, anisotropic distributions are found at the periphery of the cell, which have been attributed to actin fibre bundles. (c) Horizontal KB beam profile without and with soft-edge cleaning apertures, as used to obtain the data in (a, b, d, f). Note the steep decay of the KB profile over seven orders of magnitude! Also shown is the slight suppression of background resulting from the BS in front of the flight tube. (d) Example of an anisotropic diffraction pattern at the location indicated by the cross in (a). Scale bar:  $0.1\ \text{nm}^{-1}$ . (e) Simulated diffraction profile of two filaments crossing at an angle varied to match the data in (d). Note that the extension of strong diffraction is orthogonal to the fibre bundle axis. Scale bar:  $0.1\ \text{nm}^{-1}$ .

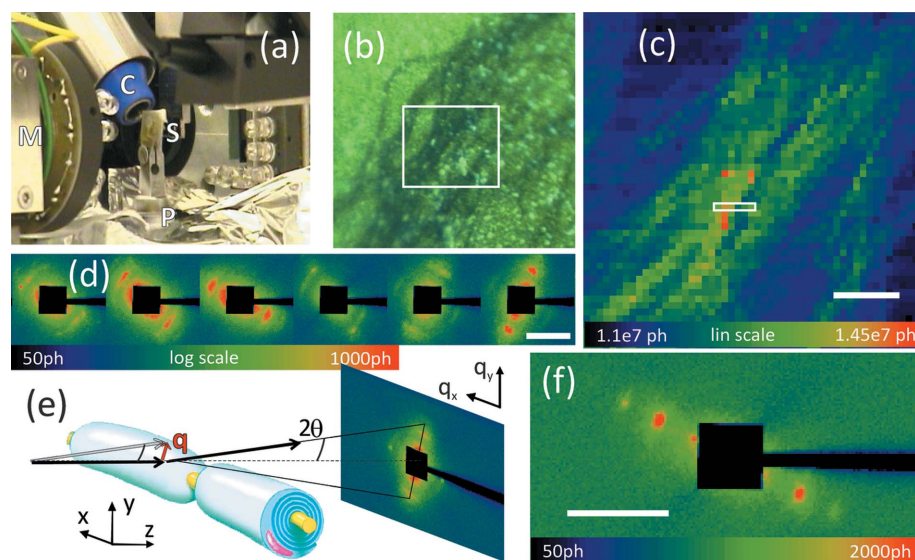
Ranvier. In the radial direction, the compact membrane structure exhibits a periodic structure with a lamellar periodicity  $d$  of around 16 nm, depending on neuron type, species and possibly state. The importance of myelin and its structure for signal conduction is shown from its important role in different neurological diseases, including multiple sclerosis. Unlike in classical myelin diffraction experiments, which average over the entire nerve, the local myelin structure becomes accessible from mappings of the diffraction signal along and across single nerve fibres. Important structural parameters such as the lamellar periodicity  $d$  (from the radial peak position), membrane orientation (from the angular orientation of diffraction peaks) and possibly parameters on the myelin order/disorder (from the peak width and intensity variations) can thus be accessed on a local scale. The requirements regarding beam preparation and instrumental settings, including nanobeam focusing and conditioning, detector dynamic range, as well as cryo-protection against radiation damage, have been addressed by Ducic *et al.* (2011). With the improvements in beam conditioning as presented here, as well as the cryojet sample environment, the requirements for advanced biological nano-diffraction experiments have now been reached, and represent a significant step ahead with respect to the diffraction data recorded before (Ducic *et al.*, 2011).

Fig. 5 shows typical diffraction signals, recorded in a recent test experiment at GINIX on freeze-dried single-fibre

preparations, by scanning at 7.9 keV photon energy with a beam size of 280 nm (vertical) and 360 nm (horizontal). To minimize damage, the sample was kept in a cryogenic nitrogen gas jet (Oxford CryoSystems). A photograph of the sample mounted on a thin foil in the cryostream is shown in Fig. 5(a); an on-axis microscope image used for alignment is shown in Fig. 5(b). The corresponding X-ray dark-field map, Fig. 5(c), shows the contour of axon fibres, which lead to strong diffraction, exemplified for several scan points in Fig. 5(d). For each scan point, a diffraction image was recorded, using a Pilatus 100K pixel detector (Dectris), positioned 329 mm behind the sample (front detector bench). In some locations, the signal and lamellar ordering was found to be high enough to record higher lamellar reflection orders; see for example Fig. 5(f).

### 5. The waveguide probe for holographic imaging

Out of the three imaging modalities supported by the optical system, in-line holographic imaging in the high-magnification/high-resolution setting is the primary purpose for which it was designed and offers unique characteristics. The object transmission function  $o$  is reconstructed from the holographic intensity recorded in the divergent wavefield exiting the waveguide (Giewekemeyer *et al.*, 2011; Bartels *et al.*, 2012). The FOV and the geometric magnification  $M = 1 + z_2/z_1$  of the in-line hologram is adjusted by the object distance from the waveguide source  $z_1$ , and the object-to-detector distance  $z_2$ , following the principle of propagation imaging in diverging (cone) beams (Wilkins *et al.*, 1996; Lagomarsino *et al.*, 1997; Mokso *et al.*, 2007). The image formation is described by  $I_z(x, y) := |\mathcal{D}_z\{p(x, y) o(x, y)\}|^2$  with the free-space Fresnel propagator  $\mathcal{D}_z$  acting on the product of  $p$  and  $o$ , and the effective propagation distance  $z = z_2/M$ .  $p$  is the probe function, corresponding to the quasi-point source of the waveguide. Reconstruction is not limited to samples of finite support, and works even for a single acquisition, which is of advantage for tomography and time-resolved imaging. In contrast to far-field CDI and ptychography, the detector pixels are filled much more evenly, similar to radiographic imaging, avoiding complications associated with a high dynamic range of the signal, and in particular pixel saturation and loss of information due to beamstops. Despite its apparent simplicity, to date only few dedicated instruments are available for this form of cone-beam holographic imaging. The central challenge arises



**Figure 5**

(a) Photograph of the sample (S) mounted on the piezo table (P) in the cryo-stream (C), with an *in situ* on-axis visible-light microscope (M). (b) View of the sample in the optical microscope (M), used for alignment and inspection during the X-ray exposure. The indicated rectangle (white lines) is scanned in (c). (c) Myelin scattering intensity map (dark-field) for scan field of  $100 \mu\text{m} \times 100 \mu\text{m}$ , in units of photon (ph) number per 50 ms acquisition time and detector pixel (region of interest around the lamellar diffraction). The real-space pixel size in (c) is  $2 \mu\text{m}$ , and hence significantly larger than the beam size for this overview image, showing several parallel nerve fibres as deposited on a polyimide foil. At each pixel a complete diffraction pattern is recorded, as exemplified for six pixels in (d), which underline the surprisingly large diversity of local structures. The black square is a shadow of the beamstop. (e) Sketch of a diffraction experiment, illustrating the scattering geometry and a typical myelin diffraction intensity distribution. (f) In some spots, the order is high enough to yield pronounced higher harmonic reflections. Scale bars: (c)  $20 \mu\text{m}$ ; (d, f)  $1 \text{nm}^{-1}$ .

from focusing. Firstly, the resolution depends on the focal spot size and corresponding numerical aperture of the cone beam. Secondly, even if reaching a sufficiently small spot size  $\Delta$ , the idealized assumption of a clean spherical wavefront as emanating from an ideal point source poses some concern. In practice, the smaller the focal spot size, the more difficult it is to avoid aberrations and tails. The magnified near-field (in-line) holograms then become strongly corrupted impeding quantitative reconstructions. This effect cannot be simply corrected for by division by the empty beam intensity distribution (Hagemann *et al.*, 2014). Instead, the complex illumination function (the ‘probe’) must then be reconstructed simultaneously with the object (Robisch & Salditt, 2013; Stockmar *et al.*, 2013), or obtained in an independent procedure (Quiney *et al.*, 2006; Williams *et al.*, 2006; Putkunz *et al.*, 2011; Abbey *et al.*, 2008) in order to determine the correct complex-valued sample transmission function  $o(x, y)$ . Importantly, a complex-valued division in the sample plane, not the standard real-valued division in the detector plane, is required to correct for a non-ideal illumination. The extra information needed for reconstruction requires increased efforts in data recording by scanning laterally or longitudinally. To avoid such complications and to enable quantitative reconstruction from single distance/single images, the approach described here provides highly coherent and well controlled spherical wavefronts emitted by X-ray waveguides (Krüger *et al.*, 2010, 2012; Neubauer *et al.*, 2014) positioned in the KB focal plane (see the sketch in Fig. 1). Waveguide mode filtering significantly reduces wavefront aberrations and increases the spatial coherence. Importantly, the waveguide transmits only the radiation modes required for the coherent imaging process, and filters out background radiation, which is absorbed in the cladding (Osterhoff & Salditt, 2011). For the propagation of a smooth (Gaussian-like) waveguide probe, the approximation  $I_z := |\mathcal{D}_z\{PO\}|^2 \simeq |\mathcal{D}_z\{P\}|^2|\mathcal{D}_z\{O\}|^2$  is well satisfied, supporting artifact-free normalization by the empty beam  $I_z^E := |\mathcal{D}_z\{P\}|^2$ , expressed by  $\bar{I}_z = I_z/I_z^E = |\mathcal{D}_z\{O\}|^2$ . The normalized intensity is thus directly related to the transmission function  $O = \exp\{-i2\pi/\lambda \int_{-\Delta t}^0 [\delta_\lambda(x, y, z) - i\beta_\lambda(x, y, z)] dz\}$  of the object with thickness  $\Delta t$  and refractive index  $n = 1 - \delta_\lambda + i\beta_\lambda$  at wavelength  $\lambda$ , in contrast to holography with unfiltered KB beams.

The magnified hologram directly represents the location and shape of the object, enabling easy sample alignment and providing a further (optional) constraint for iterative phase retrieval. Progress in fabrication of lithographic waveguide channels has helped to overcome the low efficiencies which have previously severely limited X-ray waveguide optics (Jarre *et al.*, 2005), increasing the waveguide exit flux to  $I_{\text{WG}} > 10^9$  photons  $\text{s}^{-1}$ , at a source size (FWHM) of 25.4 nm (horizontal)  $\times$  30.8 nm (vertical) in the waveguide exit plane (Bartels, 2013; Bartels *et al.*, 2015), as determined by inverting the empty beam far-field pattern by an error-reduction algorithm (Krüger *et al.*, 2012). Smaller spot sizes of around 10 nm can also be realised (Krüger *et al.*, 2012), however, at reduced flux. For highest flux, for example as required for imaging with high temporal resolution, the pure KB beam can be used for

holographic imaging; however, of course not with the same image quality and resolution.

Next to aberration-free wavefronts, suitable algorithms for quantitative image reconstruction have posed a second major challenge. Simple reconstruction based on back propagation of the measured hologram as in the original form of in-line holography (Gabor, 1948) proves to be flawed by strong artifacts. This is also known as the twin image problem of holography. Quantitative phase contrast imaging has become possible only by the advanced phase-retrieval algorithms devised in the modern era of digital holography, in particular concerning X-ray imaging (Paganin, 2006; Nugent, 2010; Quiney & Nugent, 2011). But most approaches and algorithms still relied on idealizations and linearization, based either on an expansion of  $o$  (weak specimen), leading to analytical forms of the contrast-transfer function (CTF) (Cloetens *et al.*, 1999; Turner *et al.*, 2004; Gureyev *et al.*, 2004; Langer *et al.*, 2012; Moosmann *et al.*, 2013), or on the expansion of the propagator (Bronnikov, 1999; Krenkel *et al.*, 2013), leading to the transport-of-intensity equation (TIE). Beyond the direct contrast regime  $F \gg 1$ , where the standard implementations of TIE-based reconstructions fail, or for samples which are not sufficiently weak (Guigay, 1977) to be treated by CTF-based reconstruction, further simplifications have been proposed such as a known coupling between the object’s dispersion and absorption properties (single material assumption) (Paganin *et al.*, 2002). *A priori* information such as positive definiteness (Latychevskaia & Fink, 2007) for the phase, and even more so finite support, have also proven to increase reconstruction quality (Giewekemeyer *et al.*, 2011), also for samples of general composition. More recently, we have proposed a generalized TIE approach (holo-TIE) valid for the entire range of  $F$  (Krenkel *et al.*, 2013), as well as a generalization of ptychography based on lateral and longitudinal shifts of the object in the beam, enabling simultaneous reconstruction of  $o$  and  $p$  without further constraints or restrictions (Robisch & Salditt, 2013).

X-ray holographic imaging using the optics described here has recently been demonstrated at 22 nm resolution for a test pattern, imaged with a FOV of about  $20 \mu\text{m} \times 40 \mu\text{m}$ , and for freeze-dried bacterial cells at about 53 nm resolution (Bartels *et al.*, 2015). The images revealed dense structures of the bacterial nucleoids of *Deinococcus radiodurans* attributed to compactified DNA, which were also studied tomographically (Bartels *et al.*, 2012). The dose efficiency was remarkably high, enabling quantitative phase contrast imaging of bacteria even in the hydrated and living state.

Fig. 6 illustrates coherent imaging with the waveguide probe in the (deep) holographic regime for  $F \ll 1$ , with holograms shown for (a) a test pattern, and (b) three *Deinococcus radiodurans* cells. The raw data hologram shown in (b) as recorded shows the image formation with the bacterial cells aligned in the centre of the primary beam. In contrast to far-field CDI where the centre is typically blocked by a central stop, the centre of the direct beam (waveguide probe) is the carrier of the signal and needs to be sampled at high frequency, *i.e.* with small detector pixels. The example of an

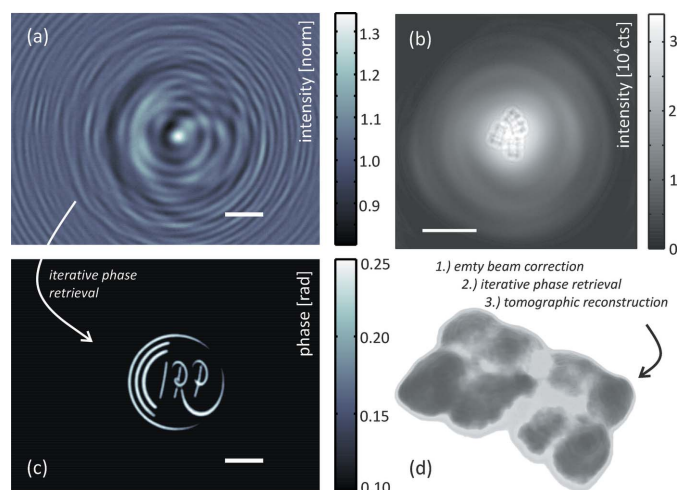


**Figure 6**

Holographic imaging with the waveguide probe. Scale bar: 585  $\mu\text{m}$  (detector plane). (a) Hologram of a test pattern after division by the empty beam. Scale bar: 6 mm (detector plane). (b) Raw data of a hologram with three *Deinococcus radiodurans* cells, showing the smooth line-shape and tails of the waveguide probe. (c) Phase reconstruction of the hologram shown in (a), with 22.4 nm pixel size. Scale bar: 2  $\mu\text{m}$ . (d) Rendered three-dimensional density distribution of a *Deinococcus radiodurans* bacteria (Bartels *et al.*, 2012), reconstructed from waveguide-based holographic tomography.

empty beam corrected hologram in (a) shows the holographic fringes with respect to the flat background (after empty beam division and raw data corrections), recorded with a test pattern milled by focused ion beam into a 200 nm-thick gold layer on 200 nm-thick  $\text{Si}_3\text{N}_4$  over a total accumulation time of 30 s at 7.9 keV photon energy, waveguide-to-object distance  $z_1 = 17.55$  mm, and detector distance  $z_1 + z_2 = 5.13$  m. Interference fringes extend all the way to the corners of the diffraction pattern indicating a high-quality hologram. The phase reconstructed from this hologram is shown in Fig. 6(c), based on the algorithms presented by Giewekemeyer *et al.* (2011) and Bartels *et al.* (2015), which enforces compact object support as well as measured intensity values. Importantly, the support information required for this algorithm is retrieved from a deterministic holographic reconstruction and thus does not need prior information such as in CDI. The raw data of a holographic recording is illustrated in Fig. 6(b) for bacteria, before empty beam correction. Waveguide-enhanced holographic imaging can readily be extended to tomography, as demonstrated for *Deinococcus radiodurans* cells by Bartels *et al.* (2012). A corresponding rendering of the three-dimensional electron density distribution is shown in Fig. 6(d). The quantitative two-dimensional and three-dimensional phase retrieval reveals dense structures which may be associated with DNA rich bacterial nucleoids.

## 6. Conclusion and outlook

A unique aspect of the compound mirror–waveguide system discussed here is the delivery of quasi-spherical wavefronts emanating from a two-dimensional X-ray waveguide exit (Salditt *et al.*, 2008; Giewekemeyer *et al.*, 2010; Krüger *et al.*,

2010), with controlled mode structure spot sizes down to sub-10 nm. The mode and coherence filtered waves are ideally suited for quantitative holographic image recording. Mode filtering minimizes wavefront distortions and artifacts encountered in many other hard X-ray focusing optics. This enables quantitative reconstruction of the object by robust phase-retrieval algorithms. By selecting the waveguide-to-sample distance, objects can be imaged at a single distance in a full-field configuration without scanning. Robust and quickly converging iterative reconstruction schemes can be applied to invert the holographic near-field diffraction patterns. Weakly scattering biological specimen can thus be phased even without exact knowledge of the illumination function. The method proved to be very dose-efficient providing images of cells at doses below  $10^5$  Gy, and takes photon noise effects into account quantitatively (Giewekemeyer *et al.*, 2011). The tomographic extension provides quantitative three-dimensional density reconstructions of biological cells and tissues (Bartels *et al.*, 2012; Olendrowitz *et al.*, 2012). To probe the three-dimensional structure of a larger specimen, the full-field holographic technique is of particular advantage, since it avoids the problem of overheads in detector readout which is pertinent in scanning three degrees of freedom (two translations, one tomographic rotation). In contrast to scanning SAXS or diffraction microscopy (ptychography), extended specimens from several cells and multicellular organisms to tissues up to the organ level of small animals can be covered in one or a few exposures, eventually enlarged by stitching. Using zoom magnification by defocus variation, the magnification and the FOV can easily be adapted and combined. At the same time the optical scheme is ideally suited for high-flux ptychographic phasing and scanning SAXS/WAXS applications, and a fast switch in imaging modality on the same sample is supported by the optical design. The advanced detection systems already tested for the KB nano-probe (Giewekemeyer *et al.*, 2014; Wilke *et al.*, 2014), but also the Eiger detector (Guizar-Sicairos *et al.*, 2014), can cope with the high flux density.

As a future direction, the described optics and imaging scheme for all imaging modalities is compatible with pink beam operations, which would increase flux by one to two orders of magnitude. For scanning nano-diffraction in SAXS or even WAXS mode as long as weakly ordered systems are considered, the intrinsic undulator bandpath of  $\Delta\lambda/\lambda \simeq 0.006$  would not be prohibitively large, and hence even weakly scattering samples such as the hydrated cell in Fig. 4 could be acquired with dwell times of  $\leq 10$  ms. Scanning with continuous motor movement and pixel detector technology for frame rates of  $\geq 100$  Hz is already available, warranting a straightforward implementation of such a fast nano-diffraction mode. Concerning radiation damage, further studies should investigate whether a ‘diffract-and-destroy’ strategy can be adopted based on increased scanning speed to outrun diffusion-limited reactions of free radicals. For ptychography, pink beam operation could bring about higher robustness and reconstruction quality, by avoiding any vibrations associated with monochromator cooling. For small spot sizes, *i.e.* in the

focal plane and super-resolution factors of  $\leq 100$ , speckle smearing by the bandpath could be neglected. A resolution of below 10 nm also for biological specimens could be a reasonable goal, but radiation damage is likely to be a show-stopper for many applications. Note that a ‘diffract-and-destroy’ strategy would be impeded by the required spatial overlap. Contrarily, waveguide-based holographic imaging is readily compatible with pink beam operations, and, since the sample is positioned out of focus, eventual radiation damage issues can be better controlled (by variation of  $z_1$ ). Full-field images such as those shown in Fig. 6 could be accumulated within a second or less. Most importantly, fractionating a 1 s exposure over 100 or even 1000 acquisitions would help to minimize vibration- or drift-induced blurring of the holograms. Each of the acquisitions would have enough signal to allow for a cross-correlation and hence a drift-corrected hologram. Since the current resolution of about 20 nm (for test structures) is certainly limited by vibrations, this could be an important step forward along with more efforts into vibration control. Finally, pink beam operation could enable tomography with the KB beam at rates of a full tomogram per second, and spatial resolution in the range of 300 nm. In addition, pink beam operation could also significantly enhance time-resolved imaging and diffraction of soft matter and biomolecular samples in the pump–probe (Reusch *et al.*, 2013) or stroboscopic scheme (Reusch *et al.*, 2013). With an expected flux of  $10^7$ – $10^8$  photons in a single bunch, nano-focusing could be combined with single-bunch imaging.

## 7. Related literature

The following references are mentioned in the supporting information: Balewski *et al.* (2004), Certified Scientific Software (2015), Leupold & Sprung (2008), Rossi *et al.* (2006), Takahashi *et al.* (2013).

## Acknowledgements

We thank Bastian Hartmann for excellent engineering support of this project, Alexey Zozulya, Fabian Westermeier and the entire PETRA III team for their outstanding and continuous support, and DESY Photon Science for beam time. We are also grateful for the many past and current collaborators and users of the setup for numerous improvements and suggestions. Financial support by the collaborative research centre 755 ‘Nanoscale Photonic Imaging’ of the Deutsche Forschungsgemeinschaft, by the German Ministry of Science and Education under project number BMBF 05K13MG4, and by the Virtual Institute VH-VI-403 ‘In situ Nano-Imaging of Biological and Chemical Processes’ of the Helmholtz Gemeinschaft is gratefully acknowledged.

## References

Abbey, B., Nugent, K. A., Williams, G. J., Clark, J. N., Peele, A. G., Pfeifer, M. A., de Jonge, M. & McNulty, I. (2008). *Nat. Phys.* **4**, 394–398.  
 Balewski, K., Brefeld, W., Decking, W., Franz, H., Rohlsberger, H. & Weckert, E. (2004). *PETRA III: A Low Emittance Synchrotron*

*Radiation Source*. Technical Report. Deutsches Elektronen-Synchrotron DESY, Hamburg, Germany.  
 Bartels, M. (2013). PhD thesis, Universität Göttingen, Germany.  
 Bartels, M., Krenkel, M., Haber, J., Wilke, R. N. & Salditt, T. (2015). *Phys. Rev. Lett.* **114**, 048103.  
 Bartels, M., Priebe, M., Wilke, R., Krüger, S., Giewekemeyer, K., Kalbfleisch, S., Olendrowitz, C. C., Sprung, M. & Salditt, T. (2012). *Opt. Nanosci.*, **1**, 10.  
 Bergemann, C., Keymeulen, H. & van der Veen, J. F. (2003). *Phys. Rev. Lett.* **91**, 204801.  
 Bronnikov, A. V. (1999). *Opt. Commun.* **171**, 239–244.  
 Bukreeva, I., Popov, A., Pelliccia, D., Cedola, A., Dabagov, S. B. & Lagomarsino, S. (2006). *Phys. Rev. Lett.* **97**, 184801.  
 Bunk, O., Bech, M., Jensen, T. H., Feidenhans'l, R., Binderup, T., Menzel, A. & Pfeiffer, F. (2009). *New J. Phys.* **11**, 123016.  
 Certified Scientific Software (2015). *Certified Scientific Software*, <http://certif.com>.  
 Chapman, H. N., Barty, A., Marchesini, S., Noy, A., Hau-Riege, S. P., Cui, C., Howells, M. R., Rosen, R., He, H., Spence, J. C. H., Weierstall, U., Beetz, T., Jacobsen, C. & Shapiro, D. (2006). *J. Opt. Soc. Am. A*, **23**, 1179–1200.  
 Cloetens, P., Ludwig, W., Baruchel, J., Van Dyck, D., Van Landuyt, J., Guigay, J. P. & Schlenker, M. (1999). *Appl. Phys. Lett.* **75**, 2912–2914.  
 Dierolf, M., Menzel, A., Thibault, P., Schneider, P., Kewish, C. M., Wepf, R., Bunk, O. & Pfeiffer, F. (2010). *Nature (London)*, **467**, 436–439.  
 Döring, F., Robisch, A., Eberl, C., Osterhoff, M., Ruhlandt, A., Liese, T., Schlenkerich, F., Hoffmann, S., Bartels, M., Salditt, T. & Krebs, H. (2013). *Opt. Express*, **21**, 19311–19323.  
 Ducić, T., Quintes, S., Nave, K.-A., Susini, J., Rak, M., Tucoulou, R., Alevra, M., Guttman, P. & Salditt, T. (2011). *J. Struct. Biol.* **173**, 202–212.  
 Feng, Y. P., Sinha, S. K., Deckman, H. W., Hastings, J. B. & Siddons, D. P. (1993). *Phys. Rev. Lett.* **71**, 537–540.  
 Gabor, D. (1948). *Nature (London)*, **161**, 777–778.  
 Giewekemeyer, K., Krüger, S. P., Kalbfleisch, S., Bartels, M., Beta, C. & Salditt, T. (2011). *Phys. Rev. A*, **83**, 023804.  
 Giewekemeyer, K., Neubauer, H., Kalbfleisch, S., Krüger, S. P. & Salditt, T. (2010). *New J. Phys.* **12**, 035008.  
 Giewekemeyer, K., Philipp, H. T., Wilke, R. N., Aquila, A., Osterhoff, M., Tate, M. W., Shanks, K. S., Zozulya, A. V., Salditt, T., Gruner, S. M. & Mancuso, A. P. (2014). *J. Synchrotron Rad.* **21**, 1167–1174.  
 Giewekemeyer, K., Wilke, R. N., Osterhoff, M., Bartels, M., Kalbfleisch, S. & Salditt, T. (2013). *J. Synchrotron Rad.* **20**, 490–497.  
 Guigay, J. P. (1977). *Optik*, **49**, 121–125.  
 Guizar-Sicairos, M., Evans-Lutterrodt, K., Isakovic, A. F., Stein, A., Warren, J. B., Sandy, A. R., Narayanan, S. & Fienup, J. R. (2010). *Opt. Express*, **18**, 18374–18382.  
 Guizar-Sicairos, M., Johnson, I., Diaz, A., Holler, M., Karvinen, P., Stadler, H.-C., Dinapoli, R., Bunk, O. & Menzel, A. (2014). *Opt. Express*, **22**, 14859–14870.  
 Guizar-Sicairos, M., Narayanan, S., Stein, A., Metzler, M., Sandy, A. R., Fienup, J. R. & Evans-Lutterrodt, K. (2011). *Appl. Phys. Lett.* **98**, 111108.  
 Gureyev, T. E., Pogany, A., Paganin, D. M. & Wilkins, S. W. (2004). *Opt. Commun.* **231**, 53–70.  
 Hagemann, J., Robisch, A.-L., Luke, D. R., Homann, C., Hohage, T., Cloetens, P., Suhonen, H. & Salditt, T. (2014). *Opt. Express*, **22**, 11552–11569.  
 Hignette, O., Cloetens, P., Rostaing, G., Bernard, P. & Morawe, C. (2005). *Rev. Sci. Instrum.* **76**, 063709.  
 Hönig, S., Hoppe, R., Patommel, J., Schropp, A., Stephan, S., Schöder, S., Burghammer, M. & Schroer, C. G. (2011). *Opt. Express*, **19**, 16324–16329.  
 Jarre, A., Fuhse, C., Ollinger, C., Seeger, J., Tucoulou, R. & Salditt, T. (2005). *Phys. Rev. Lett.* **94**, 074801.

- Johnson, I., Bergamaschi, A., Buitenhuis, J., Dinapoli, R., Greiffenberg, D., Henrich, B., Ikonen, T., Meier, G., Menzel, A., Mozzanica, A., Radicci, V., Satapathy, D. K., Schmitt, B. & Shi, X. (2012). *J. Synchrotron Rad.* **19**, 1001–1005.
- Kalbfleisch, S. (2012). PhD thesis, Universität Göttingen, Germany.
- Kalbfleisch, S., Neubauer, H., Krüger, S. P., Bartels, M., Osterhoff, M., Mai, D. D., Giewekemeyer, K., Hartmann, B., Sprung, M. & Salditt, T. (2011). *AIP Conf. Proc.* **1365**, 96–99.
- Kewish, C. M., Guizar-Sicairos, M., Liu, C., Qian, J., Shi, B., Benson, C., Khounsary, A. M., Vila-Comamala, J., Bunk, O., Fienup, J. R., Macrander, A. T. & Assoufid, L. (2010b). *Opt. Express*, **18**, 23420–23427.
- Kewish, C. M., Thibault, P., Dierolf, M., Bunk, O., Menzel, A., Vila-Comamala, J., Jefimovs, K. & Pfeiffer, F. (2010a). *Ultramicroscopy*, **110**, 325–329.
- Kraft, P., Bergamaschi, A., Broennimann, Ch., Dinapoli, R., Eikenberry, E. F., Henrich, B., Johnson, I., Mozzanica, A., Schlepütz, C. M., Willmott, P. R. & Schmitt, B. (2009). *J. Synchrotron Rad.* **16**, 368–375.
- Krenkel, M., Bartels, M. & Salditt, T. (2013). *Opt. Express*, **21**, 2220–2235.
- Krüger, S. P., Giewekemeyer, K., Kalbfleisch, S., Bartels, M., Neubauer, H. & Salditt, T. (2010). *Opt. Express*, **18**, 13492–13501.
- Krüger, S. P., Neubauer, H., Bartels, M., Kalbfleisch, S., Giewekemeyer, K., Wilbrandt, P. J., Sprung, M. & Salditt, T. (2012). *J. Synchrotron Rad.* **19**, 227–236.
- Lagomarsino, S., Cedola, A., Cloetens, P., Di Fonzo, S., Jark, W., Soullié, G. & Riekkel, C. (1997). *Appl. Phys. Lett.* **71**, 2557–2559.
- Langer, M., Pacureanu, A., Suhonen, H., Grimal, Q., Cloetens, P. & Peyrin, F. (2012). *PLoS ONE*, **7**, e35691.
- Latychevskaia, T. & Fink, H.-W. (2007). *Phys. Rev. Lett.* **98**, 233901.
- Leupold, O. & Sprung, M. (2008). *Coherence Beamline at PETRA III – Beamline Design Report*. Technical Report. Deutsches Elektronen-Synchrotron DESY, Hamburg, Germany.
- Llopart, X., Campbell, M., Dinapoli, R., San Segundo, D. & Pernigotti, E. (2002). *IEEE Trans. Nucl. Sci.* **49**, 2279–2283.
- Mastropietro, F., Carbone, D., Diaz, A., Eymery, J., Sentenac, A., Metzger, T. H., Chamard, V. & Favre-Nicolin, V. (2011). *Opt. Express*, **19**, 19223–19232.
- Matsuyama, S., Mimura, H., Yumoto, H., Sano, Y., Yamamura, K., Yabashi, M., Nishino, Y., Tamasaku, K., Ishikawa, T. & Yamauchi, K. (2006). *Rev. Sci. Instrum.* **77**, 103102.
- Miao, J., Charalambous, P., Kirz, J. & Sayre, D. (1999). *Nature (London)*, **400**, 342–344.
- Mimura, H., Handa, S., Kimura, T., Yumoto, H., Yamakawa, D., Yokoyama, H., Matsuyama, S., Inagaki, K., Yamamura, K., Sano, Y., Tamasaku, K., Nishino, Y., Yabashi, M., Ishikawa, T. & Yamauchi, K. (2010). *Nat. Phys.* **6**, 122–125.
- Mimura, H., Kimura, T., Yokoyama, H., Yumoto, H., Matsuyama, S., Tamasaku, K., Koumura, Y., Yabashi, M., Ishikawa, T. & Yamauchi, K. (2011). *AIP Conf. Proc.* **1365**, 13–17.
- Mokso, R., Cloetens, P., Maire, E., Ludwig, W. & Buffière, J. (2007). *Appl. Phys. Lett.* **90**, 144104.
- Moosmann, J., Ershov, A., Altapova, V., Baumbach, T., Prasad, M. S., LaBonne, C., Xiao, X., Kashef, J. & Hofmann, R. (2013). *Nature (London)*, **497**, 374–377.
- Neubauer, H., Hoffmann, S., Kanbach, M., Haber, J., Kalbfleisch, S., Krüger, S. P. & Salditt, T. (2014). *J. Appl. Phys.* **115**, 214305.
- Nugent, K. A. (2010). *Adv. Phys.* **59**, 1–99.
- Olendrowitz, C., Bartels, M., Krenkel, M., Beerlink, A., Mokso, R., Sprung, M. & Salditt, T. (2012). *Phys. Med. Biol.* **57**, 5309–5323.
- Osterhoff, M. & Salditt, T. (2011). *New J. Phys.* **13**, 103026.
- Paganin, D. M. (2006). *Coherent X-ray Optics*. Oxford University Press.
- Paganin, D., Mayo, S. C., Gureyev, T. E., Miller, P. R. & Wilkins, S. W. (2002). *J. Microsc.* **206**, 33–40.
- Pennicard, D., Lange, S., Smoljanin, S., Hirsemann, H. & Graafsma, H. (2012). *J. Instrum.* **7**, C11009.
- Pfeiffer, F., David, C., Burghammer, M., Riekkel, C. & Salditt, T. (2002). *Science*, **297**, 230–234.
- Priebe, M., Bernhardt, M., Blum, C., Tarantola, M., Bodenschatz, E. & Salditt, T. (2014). *Biophys. J.* **107**, 2662–2673.
- Putkunz, C. T., Clark, J. N., Vine, D. J., Williams, G. J., Pfeifer, M. A., Balaur, E., McNulty, I., Nugent, K. A. & Peele, A. G. (2011). *Phys. Rev. Lett.* **106**, 013903.
- Quiney, H. M. (2010). *J. Mod. Opt.* **57**, 1109–1149.
- Quiney, H. M. & Nugent, K. A. (2011). *Nat. Phys.* **7**, 142–146.
- Quiney, H. M., Peele, A. G., Cai, Z., Paterson, D. & Nugent, K. A. (2006). *Nat. Phys.* **2**, 101–104.
- Reusch, T., Mai, D., Osterhoff, M., Khakulin, D., Wulff, M. & Salditt, T. (2013). *Phys. Rev. Lett.* **111**, 118102.
- Robisch, A.-L. & Salditt, T. (2013). *Opt. Express*, **21**, 23345–23357.
- Rodenburg, J. (2008). *Adv. Imaging Electron Phys.* **150**, 87–184.
- Rodenburg, J. M., Hurst, A. C., Cullis, A. G., Dobson, B. R., Pfeiffer, F., Bunk, O., David, C., Jefimovs, K. & Johnson, I. (2007). *Phys. Rev. Lett.* **98**, 034801.
- Rossi, L., Fischer, P., Rohe, T. & Wermes, N. (2006). *Pixel Detectors: From Fundamentals to Applications*. Berlin: Springer.
- Ruhlandt, A., Liese, T., Radisch, V., Krüger, S. P., Osterhoff, M., Giewekemeyer, K., Krebs, H. U. & Salditt, T. (2012). *AIP Adv.* **2**, 012175.
- Sakdinawat, A. & Attwood, D. (2010). *Nat. Photon.* **4**, 840–848.
- Salditt, T., Kalbfleisch, S., Osterhoff, M., Krüger, S. P., Bartels, M., Giewekemeyer, K., Neubauer, H. & Sprung, M. (2011). *Opt. Express*, **19**, 9656–9675.
- Salditt, T., Krüger, S. P., Fuhse, C. & Bähzt, C. (2008). *Phys. Rev. Lett.* **100**, 184801.
- Schroer, C. G. & Falkenberg, G. (2014). *J. Synchrotron Rad.* **21**, 996–1005.
- Schropp, A., Boye, P., Feldkamp, J. M., Hoppe, R., Patommel, J., Samberg, D., Stephan, S., Giewekemeyer, K., Wilke, R. N., Salditt, T., Gulden, J., Mancuso, A. P., Vartanyants, I. A., Weckert, E., Schöder, S., Burghammer, M. & Schroer, C. G. (2010). *Appl. Phys. Lett.* **96**, 091102.
- Stockmar, M., Cloetens, P., Zanette, I., Enders, B., Dierolf, M., Pfeiffer, F. & Thibault, P. (2013). *Sci. Rep.* **3**, 1927.
- Takahashi, Y., Nishino, Y., Tsutsumi, R., Zettsu, N., Matsubara, E., Yamauchi, K. & Ishikawa, T. (2010). *Phys. Rev. B*, **82**, 214102.
- Takahashi, Y., Suzuki, A., Furutaku, S., Yamauchi, K., Kohmura, Y. & Ishikawa, T. (2013). *Appl. Phys. Lett.* **102**, 094102.
- Tate, M. W., Chamberlain, D., Green, K. S., Philipp, H. T., Purohit, P., Strohman, C. & Gruner, S. M. (2013). *J. Phys. Conf. Ser.* **425**, 062004.
- Thibault, P., Dierolf, M., Menzel, A., Bunk, O., David, C. & Pfeiffer, F. (2008). *Science*, **321**, 379–382.
- Thibault, P. & Elser, V. (2010). *Annu. Rev. Condens. Matter Phys.* **1**, 237–255.
- Trueb, P., Sobott, B. A., Schnyder, R., Loeliger, T., Schneebeli, M., Kobas, M., Rassool, R. P., Peake, D. J. & Broennimann, C. (2012). *J. Synchrotron Rad.* **19**, 347–351.
- Turner, L., Dhal, B., Hayes, J., Mancuso, A., Nugent, K., Paterson, D., Scholten, R., Tran, C. & Peele, A. (2004). *Opt. Express*, **12**, 2960–2965.
- Weinhausen, B. & Köster, S. (2013). *Lab Chip*, **13**, 212–215.
- Weinhausen, B., Nolting, J.-F., Olendrowitz, C., Langfahl-Klabes, J., Reynolds, M., Salditt, T. & Köster, S. (2012). *New J. Phys.* **14**, 085013.
- Weinhausen, B., Saldanha, O., Wilke, R. N., Dammann, C., Priebe, M., Burghammer, M., Sprung, M. & Köster, S. (2014). *Phys. Rev. Lett.* **112**, 088102.
- Wilke, R. N., Hoppert, M., Krenkel, M., Bartels, M. & Salditt, T. (2015). *J. Appl. Cryst.* **48**, 464–476.
- Wilke, R. N., Priebe, M., Bartels, M., Giewekemeyer, K., Diaz, A., Karvinen, P. & Salditt, T. (2012). *Opt. Express*, **20**, 19232–19254.

- Wilke, R. N., Vassholz, M. & Salditt, T. (2013). *Acta Cryst.* **A69**, 490–497.
- Wilke, R. N., Wallentin, J., Osterhoff, M., Pennicard, D., Zozulya, A., Sprung, M. & Salditt, T. (2014). *Acta Cryst.* **A70**, 552–562.
- Wilkins, S. W., Gureyev, T. E., Gao, D., Pogany, A. & Stevenson, A. W. (1996). *Nature (London)*, **384**, 335–338.
- Williams, G. J., Quiney, H. M., Dhal, B. B., Tran, C. Q., Nugent, K. A., Peele, A. G., Paterson, D. & de Jonge, M. D. (2006). *Phys. Rev. Lett.* **97**, 025506.
- Zwanenburg, M. J., Peters, J. F., Bongaerts, J. H. H., de Vries, S. A., Abernathy, D. L. & van der Veen, J. F. (1999). *Phys. Rev. Lett.* **82**, 1696–1699.